nature portfolio

https://doi.org/10.1038/s41567-021-01219-x

# Supplementary information

# Two-fold symmetric superconductivity in few-layer $NbSe_2$

In the format provided by the
authors and unedited

# Supplementary Information

## Two-fold symmetric superconductivity in few-layer $NbSe_2$

Alex Hamill[1†], Brett Heischmidt[1†], Egon Sohn[2,3†], Daniel Shaffer[1], Kan-Ting Tsai[1], Xi Zhang[1], Xiaoxiang Xi[4], Alexey Suslov[5], Helmuth Berger[6], László Forró[6], Fiona J. Burnell[1], Jie Shan[3,7], Kin Fai Mak[3,7], Rafael M. Fernandes[1], Ke Wang[1*] and Vlad S. Pribiag[1*]

*[1]School of Physics and Astronomy, University of Minnesota, Minneapolis, MN, USA*

*[2]Department of Physics, The Pennsylvania State University, University Park, PA, USA*

*[3]Department of Physics and School of Applied and Engineering Physics, Cornell University, Ithaca, NY, USA*

*[4]National Laboratory of Solid State Microstructures, School of Physics, and Collaborative Innovation Center of Advanced Microstructures, Nanjing University, Nanjing, China*

*[5]National High Magnetic Field Laboratory, Tallahassee, FL, USA*

*[6]Institute of Condensed Matter Physics, Ecole Polytechnique Fédérale de Lausanne, Lausanne, Switzerland*

*[7]Kavli Institute at Cornell for Nanoscale Science, Ithaca, NY, USA*

**S1. Cant angle analysis**

We rule out the possibility that the observed two-fold modulation might have been caused by an out-of-plane component of the applied field, which would have oscillated with the same periodicity due to an unintentional cant of the sample plane with respect to the field rotation plane. The geometry of the canted sample and pertinent parameters are shown in Figure S1.1. The perpendicular field is proportional to $|\sin(\theta + \theta_0)|$, where $\theta_0$ is the angle needed for the field to be totally in the plane of the sample. The voltage response is also proportional to the perpendicular field for moderate $R/R_N$ (Figure S1.2), so the voltage response to an out-of-plane field should be proportional to $|\sin(\theta + \theta_0)|$.

We carried out fits for $\sin[2(\theta + \theta_0)]$ and $|\sin(\theta + \theta_0)|$ to determine the major cause of the sample's response (Figures S1.3 a-d). Moreover, a control test was performed with the same sample, but introducing an intentional (~7°) cant by using a $SiO_x$ chip as shim (Figures S1.3 e-h). We find that $|\sin(\theta + \theta_0)|$ fits the 7° cant data well, and the fit is clearly better than that for $\sin[2(\theta + \theta_0)]$. This demonstrates that magneto-resistance data does take on a $|\sin(\theta + \theta_0)|$ form in the presence of a tilted sample. By comparison, the data with no intentional cant (as in the main text) is fit best by $\sin[2(\theta + \theta_0)]$ and does not fit well to $|\sin(\theta + \theta_0)|$, excluding the possibility that the effects reported in the main text are due to an accidental tilt of the sample with respect to the field plane. This is further supported by our observations in one sample that the angle of minimum resistance of the twofold oscillations was affected by temperature and field modulation (Figure 2), which is inconsistent with the view of these oscillations being caused by misalignment (further covered in S3). A small putative misalignment angle could in principle give rise to additional angular including of similar form to our signal. However, note that when the sample is intentionally canted, the angle of the minimum resistance (due to intentional cant) is very different from the angle of minimum resistance observed in the same sample when no cant is present (cf. Figs. S1.3 a-d with Figs. S1.3 e-h), instead aligning with the placement of the shim rather than the geometry of the flake. This, along with analysis of the requisite misalignment angle (see Supplementary Section 2) and dependence of phase on sample orientation and not equipment setup (Supplementary Section 5) strongly rules out the possibility that canting would play a role for the observed two-fold anisotropy reported in the main text.

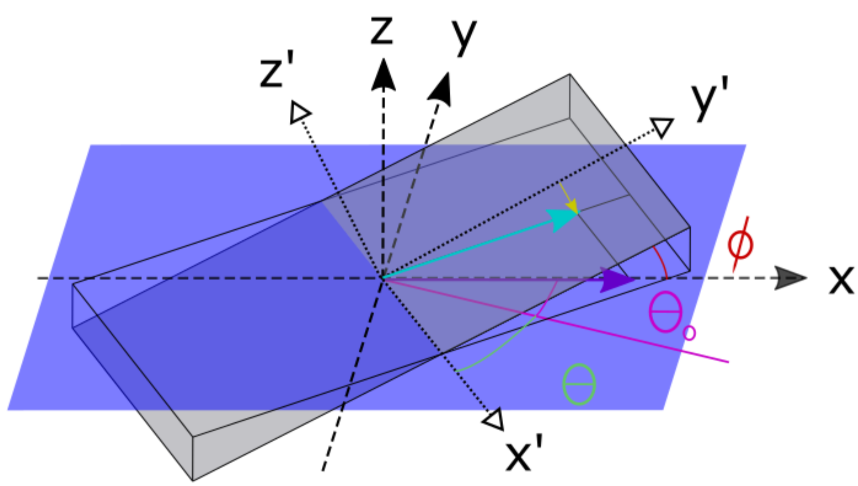


**Figure S1.1. Geometry of a canted sample**. The field lies in the x-y plane, and the sample in the x'-y' plane. The field component perpendicular to the plane of the sample takes the form $\mu_0 H|\sin(\theta + \theta_0)|\ \sin(\phi)$. Here, $\theta$ is the angle in the x-y plane, $\theta_0$ is the angle at which the field lies entirely in the plane of the sample (x'-y'), and $\phi$ is the sample's cant angle from the plane in which the field rotates (angle between the x-y and x'-y' planes). The field plane is blue, and the sample plane is grey. $\mu_0$H, $\mu_0\sin(\theta + \theta_0)$and $\mu_0$H$|\sin(\theta + \theta_0)|\sin(\phi)$ are indicated by purple, light blue and yellow arrows, respectively.

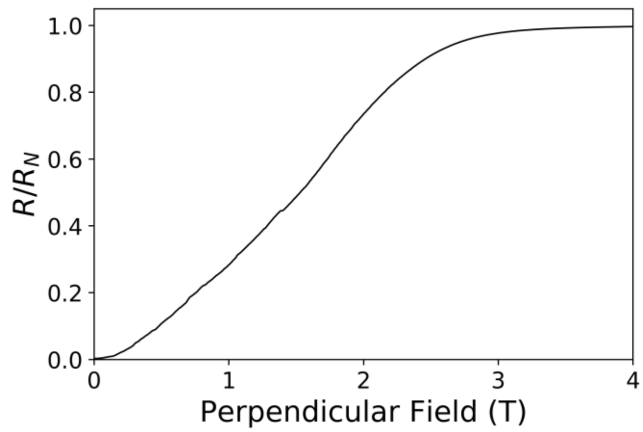


**Figure S1.2. Magnetoresistance characterization for out-of-plane sweep using Device 1**. For a range of moderate $\mathrm{R/R_N}$, resistance is roughly linear with perpendicular field (T=1.8K).

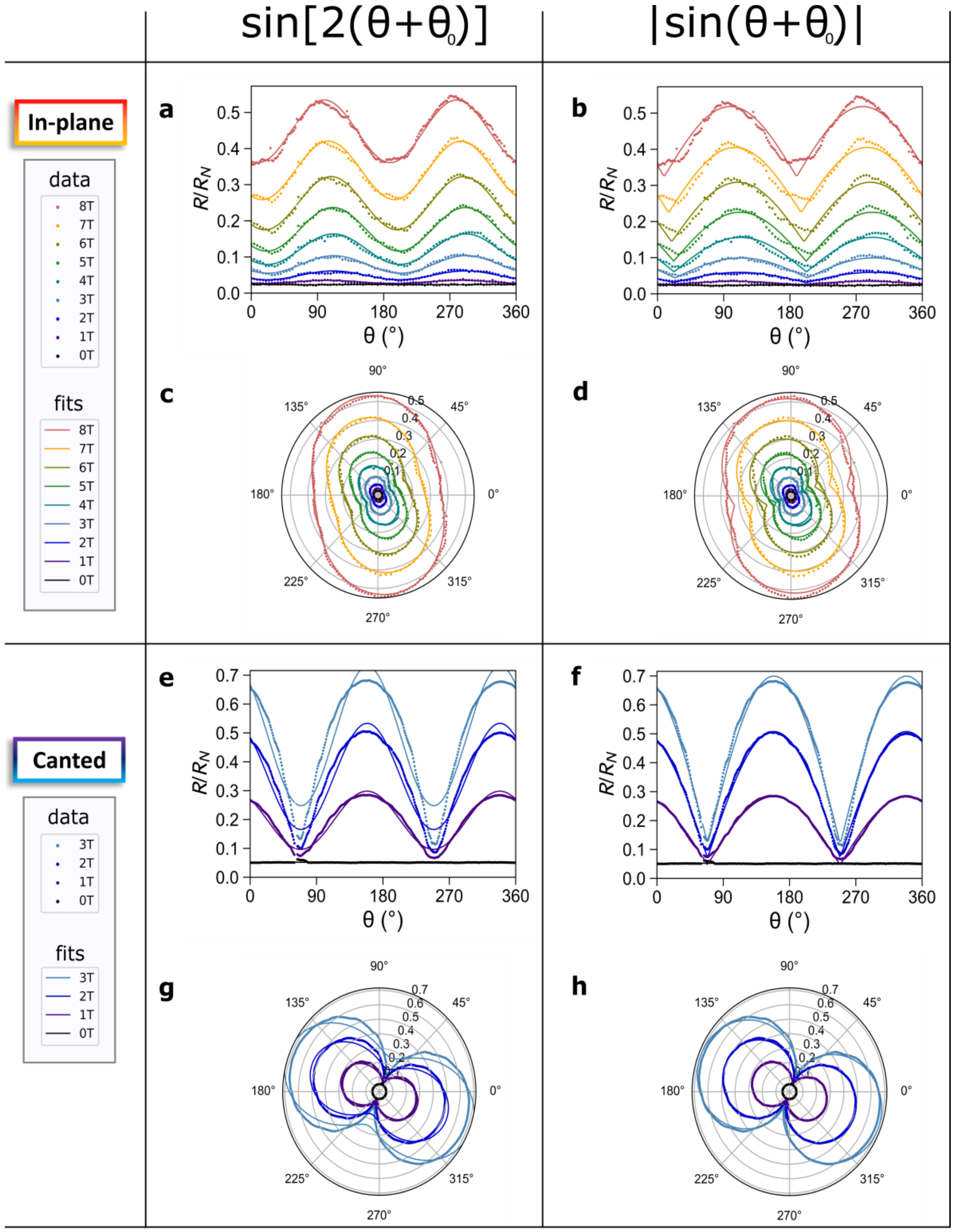


**Figure S1.3. Data are qualitatively different between canted and non-canted samples**. **a-d**: Device 1 with no cant. **a, c**: Fits to sin[2(θ + θ₀)]. **b, d**: Fits to |sin(θ + θ₀)|. **e-h.**: Device 1 with intentional cant. **e, g**: Fits to sin[2(θ + θ₀)]. **f, h**: Fits to |sin(θ + θ₀)|. Radial axis for polar plots is $R/R_N$. In all panels, experimental data are shown by discrete points and fits by solid lines. Note that when the sample is intentionally canted (e-h), the angle of the minimum resistance is very different from the angle of minimum resistance observed in the same sample when no cant is present (a-d), further ruling out the possibility that canting would play a role for the observed two-fold anisotropy reported in the main text.

**S2. Quantitative analysis of magneto-resistance to exclude plane misalignment**

The general model for misalignment-induced magnetoresistance oscillations is shown in Figure S2a where, due to a putative misalignment angle $\phi$, the normal vector $\hat{\mathrm{n}}$ of the sample would precess in a cone with in-plane rotation. This would lead to resistance maxima at the two angles corresponding to max out-of-plane field $\mathrm{H}_{\perp}$, due to thin superconductors being more sensitive to out-of-plane fields than in-plane fields due to vortex formation. By finding the hypothetical misalignment angle corresponding to the fluctuations in our data and comparing them to the estimated magnitude of actual misalignment, we show that the observed magnetoresistance oscillations are not attributable to misalignment-induced effects.

To determine the minimum hypothetical cant angle, we first calibrated the dependence of the resistance on an actual out-of-plane applied field (Fig. S2c). We then used this calibration to estimate what magnitude of out-of-plane applied field would be necessary to obtain the resistance oscillation measured with the field nominally fully in-plane (Fig. S2b). This would correspond to the maximum out-of-plane field mentioned above, which can be related to the applied field and hypothetical cant angle through the relation $\mathrm{H}_{\perp} = \mathrm{H}_{\mathrm{ext}}\sin(\phi)$ (see Fig. S2a). Comparing the associated fields in S2b,c, one gets an associated minimum putative misalignment $\phi \approx 2.44°$. This is much higher than the potential misalignment found through image analysis of the substrate-sample holder interface, which showed an estimated $\phi$ on the order of tenths of a degree. Although potential misalignment may also arise between the sample holder, probe, magnet, etc. for a given measurement system, this net contribution is found to be negligible due to the consistent two-fold angular dependence and alignment of the signal with the $NbSe_2$ flake's long, straight edge across measurement systems at Minnesota, Cornell, and MagLab. In addition, the hBN-$SiO_2$ and hBN-$NbSe_2$ interfaces are highly unlikely to host this misalignment due to the associated nm-scale topographic variation and $\mu\mathrm{m}$ length scale of the sample. As a result, it is very unlikely that an accidental misalignment between the applied field and the sample plane can be the origin of the observed two-fold anisotropy reported in this work.

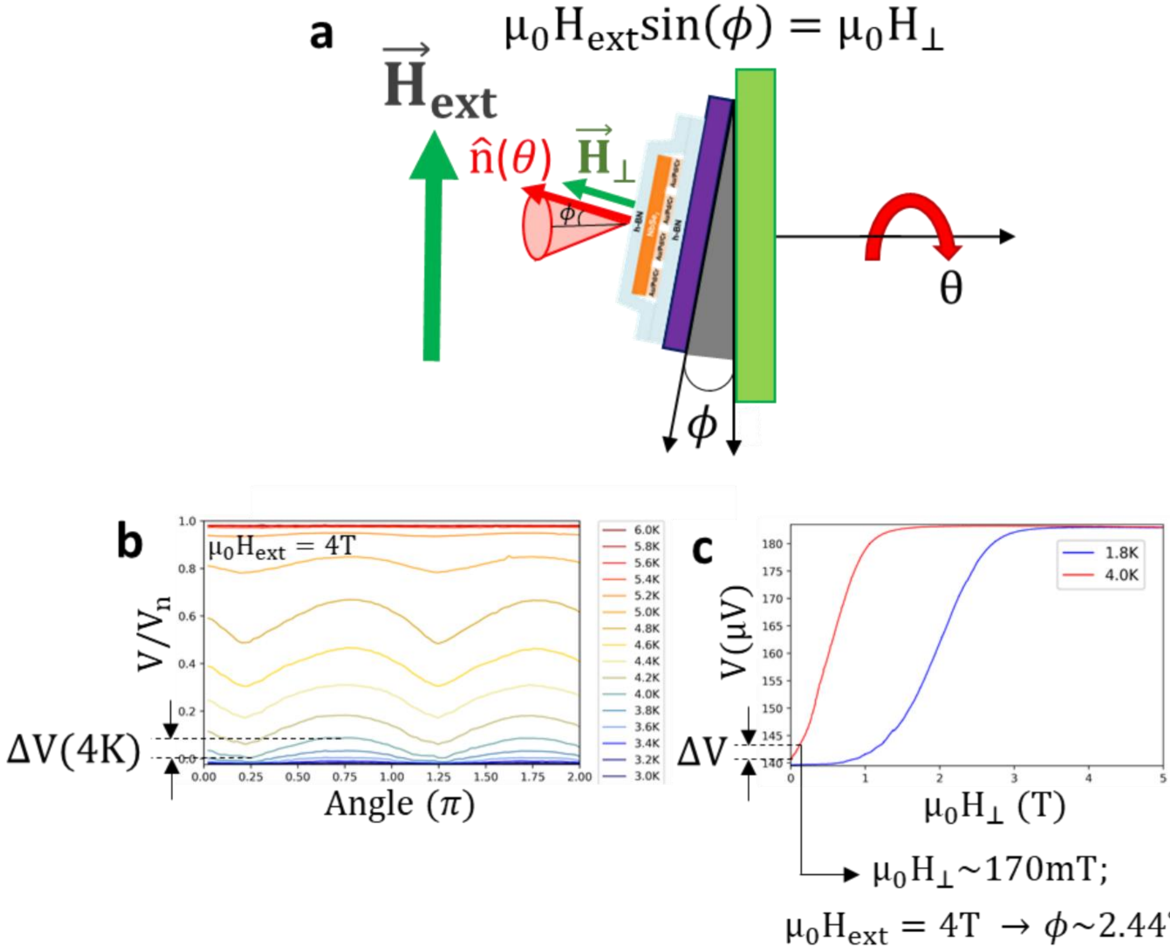


**Figure S2. Quantitative analysis of magneto-resistance to exclude plane misalignment. a.** Schematic showing geometry of setup with putative sample cant angle of $\phi$. **b.** Temperature-dependent data from Device 1 in an in-plane 4T field. **c.** Magnetoresistance of out-of-plane field sweep (three-point measurement using an a.c. current of $1\mu A$).

**S3. Shifting minima**

Another piece of evidence against an out-of-plane effect was a shifting minimum angle in the data. For a purely out-of-plane effect, no shift should be expected – this is confirmed in Figure S3 for the canted Device 1, whose minima had a range of 4° (the resolution of the measurement). Instead, Device 1 without a cant showed a minimum range of 16° for temperature dependence with a general trend to the left, and the field dependence shows a range of 32°. Notable is that this phase shift with both temperature and field modulation implies a dependence on location along the superconducting transition, rather than being due to extrinsic effects.

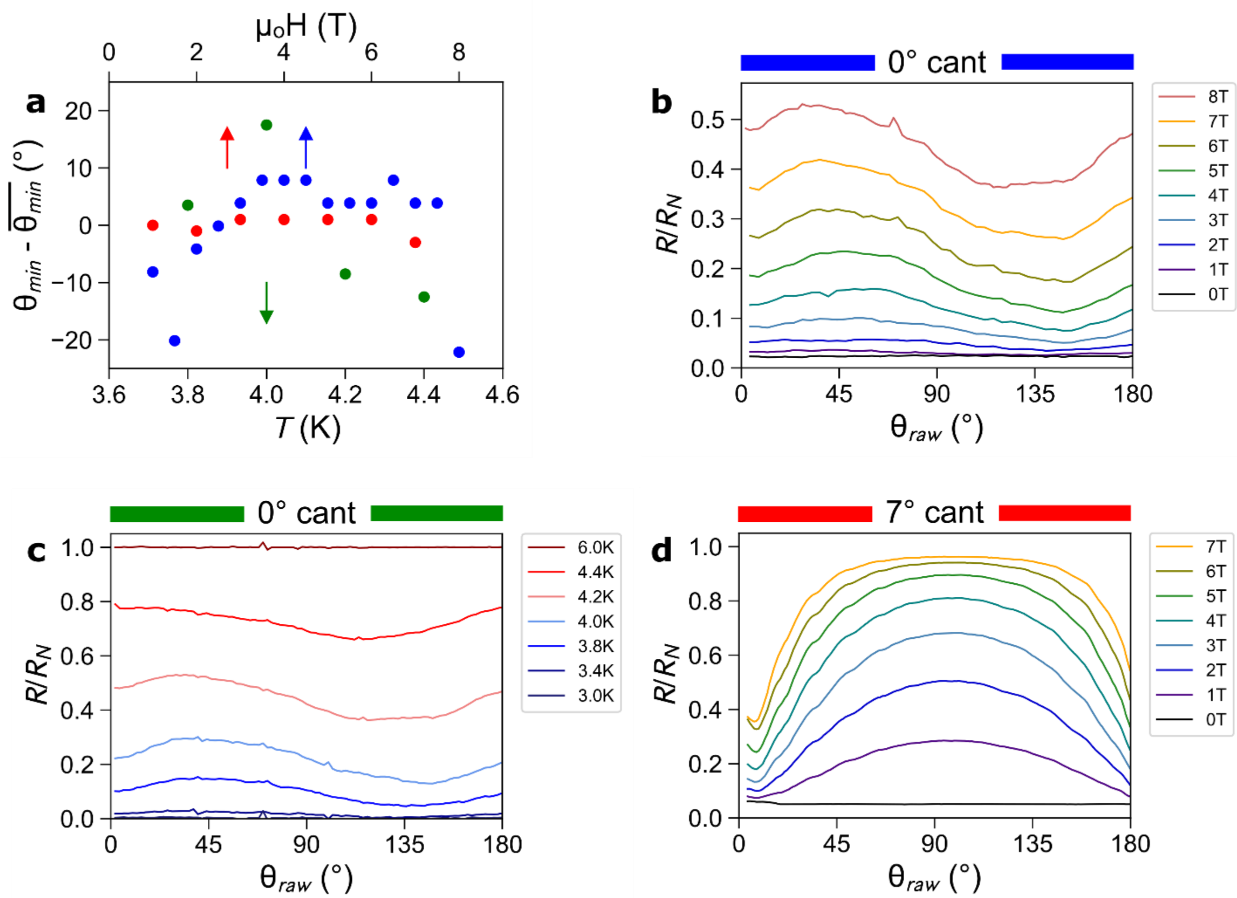


**Figure S3. Magnetoresistance minimum shift present for 0° cant, absent for 7° cant. a**. Angle at which minimum of magnetoresistance occurs for the three cases shown in panels **b**-**d**, centered around each set's average minimum angle. **b.** Field dependence of Device 1 with 0° cant (average minimum: 144°). **c.** Temperature dependence of Device 1 with 0° cant (average minimum: 133°). **d.** Field dependence of Device 1 with 7° cant (average minimum: 10°). The minimum for the 7° cant shifts very little (almost not at all) compared to that of the 0° cant. Note: the data for the 0° cant is the raw data of that shown in the main text.

**S4. Characterization of Device 3.**

Device 3 was made from a 5-layer $NbSe_2$ sample, the same as Device 1. The R vs. T (Figure S4a) for this sample showed an $\mathrm{R_N}$ of 20.4Ω and $\mathrm{T_c}$ ≈6.2K. This gives a superconducting gap $\Delta \approx 1.76\mathrm{k_B T_c} \approx$ 0.94 meV. Although the transition width is wider than in Device 1 and less uniform at low resistances, the magnetoresistance and effective critical field data were taken at a smooth part of the transition ($R \approx 0.35R_N$ to $R \approx 0.6R_N$) and showed no anomalies. Note that the step in the R vs. T curve near 3.7K is suggestive of the presence of a monolayer in part of the sample.

Resistance dependence on perpendicular and parallel fields were also studied at 0.5K (Figure S4b). The out-of-plane and in-plane upper critical fields were approximately 4T and 27T, respectively. These two measurements were taken on the same holder, and immediately following one another, but with the holder turned 90° from the first to second measurement such that the rotation in-plane with the field became a rotation out-of-plane.

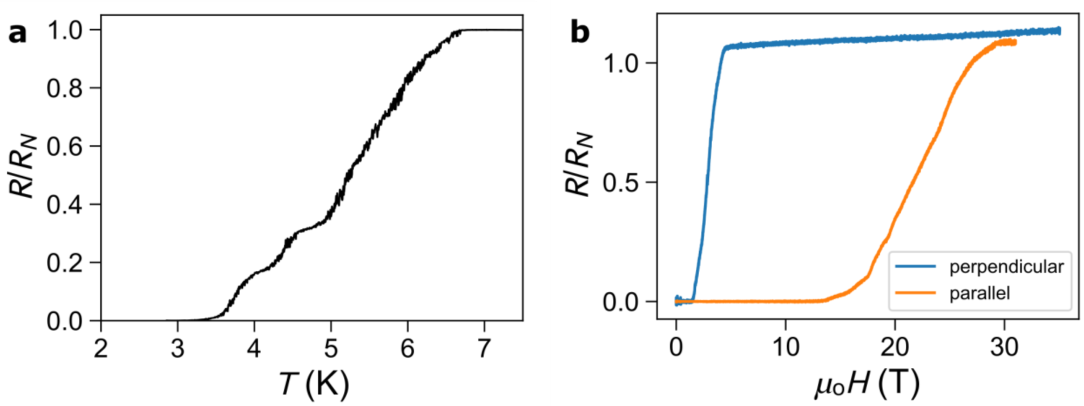


**Figure S4. Characterization for Device 3**. **a.** Normalized R vs. T ($R_N = 20.4\ \Omega$). **b.** Normalized R vs. magnetic field for the cases when the field is parallel or perpendicular to the sample.

**S5. Directional Analysis of Magnetotransport across multiple devices.**

Directions of current and the long, straight edge of the $NbSe_2$ flakes (denoted as $\theta = 0°$) are shown in Figures S5a-c, along with images of the corresponding $NbSe_2$ flakes as guides to the eye. It can be seen that there is no correlation between the angle at which the minimum in resistance is observed and the direction of the average current flow (the same applied for the direction corresponding to the associated voltage probes, not shown). Across all magneto-transport and Co/Pt tunnel junction samples, the resistance extrema correspond with the long, straight edge axis of the $NbSe_2$ flakes. Figure S5d shows the associated magnetoresistance oscillations measured in each device.

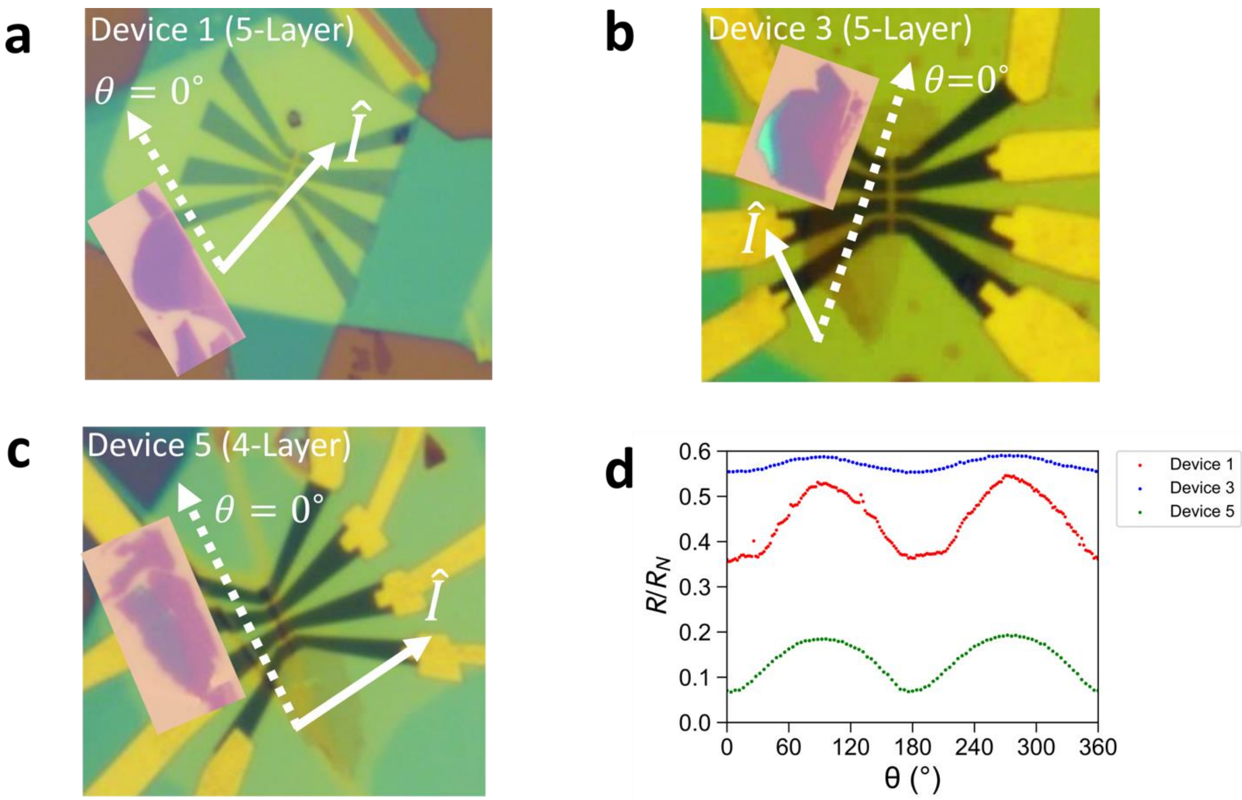


**Figure S5. Directional analysis of magnetotransport across several devices**. **a.-c**. Images of Devices 1, 3, and 5, along with the associated current directions and $NbSe_2$ long, straight edge directions (defined as $\theta = 0°$). Images of the $NbSe_2$ flakes are provided as guides to the eye. **d.** Plot of the magnetoresistance oscillations It can be seen in each case that $R_{min}$ occurs when the applied field aligns with the long, straight edge of the $NbSe_2$ flake, defined as $\theta = 0°$, and is independent of current direction. Note that increase in $\theta$ corresponds to counterclockwise rotation of the in-plane field.

**S6. Further analysis of current direction with respect to signal.**

The association of current direction with minima location is addressed. Figure S6 shows an analysis of Device 3, but as measured at the University of Minnesota. Despite a change of average current direction by 20-45 degrees, the angles of resistance minima do not shift. The local minima are identical (68° and 252°). Further, when fit to $\sin(2\theta - \varphi)$, $\varphi$ =65° for the "1 to 4" configuration, whereas $\varphi$ =71° for the "7 to 4" configuration. The difference is comparable to the angular resolution of the data (4°) and multiple times smaller than the change in current direction. The independence of resistance minimum with the current direction, in addition to complementary evidence given in S5, gives evidence against vortex physics being the primary cause of the character of the observed effect.

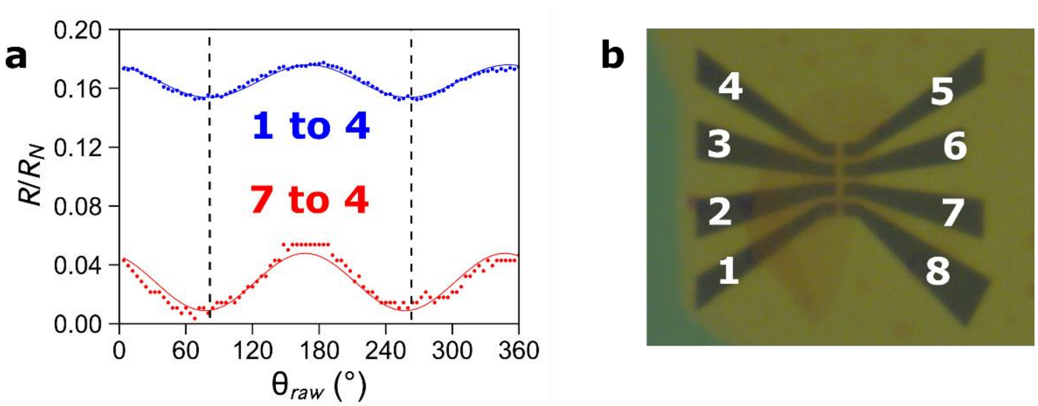


**Figure S6. Contact arrangement analysis for Device 3.** "1 to 4" indicates the current is driven from contact 1 to contact 4, and voltage is measured across contacts 2 and 3. "7 to 4" indicates the current is driven from contact 7 to contact 4, and the voltage is measured between contacts 5 and 6. In both cases, the local minima and maxima lie at approximately the same angular values within experimental uncertainty. $\theta_{raw}$ corresponds to the angle measured with respect to the cryostat. Data are points, and fits to $\sin(2\theta - \varphi)$ are thin solid lines. Vertical dashed lines go through the minima of the fit to "1 to 4," and show close alignment with the minima of the fit to "7 to 4." Both measurements were taken in the same cooldown, with the same sample orientation.

**S7. Analysis of Signal Dependence on Contact Geometry**

Here we compare data from the eventual contact geometry used for the paper (Device 1) with our initial geometry (Device 6). The twofold signal is apparent despite the varying geometry.

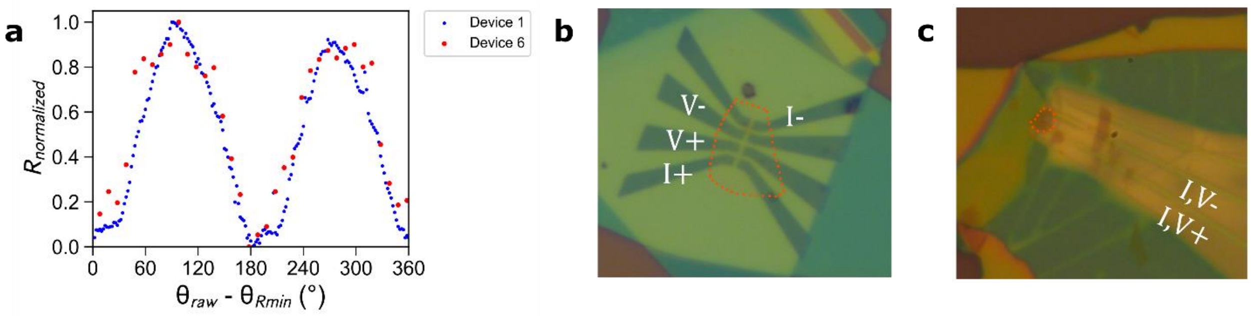


**Figure S7. Signal is independent of contact geometry. a.** Representative data for Devices 1 and 6, hBN-encapsulated magneto-transport samples based on five-layer $NbSe_2$. The resistance is normalized with 1.0 being maximum and 0.0 being minimum; a zero normalized resistance is a finite actual resistance. **b.** Device 1. **c.** Device 6, using a two-point measurement configuration.

## S8. No Hysteresis in Rotation Direction

No hysteresis in the signal is found with respect to rotation direction for Device 1. Two temperatures are shown below, with five runs compiled for each direction (twenty runs total).

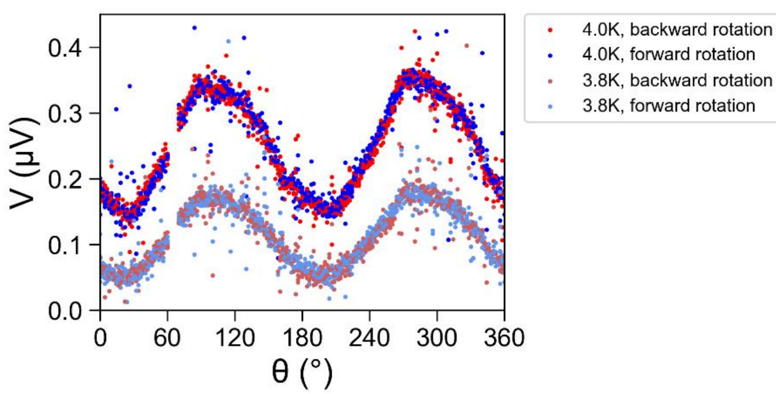


**Figure S8. Hysteresis due to rotation direction is absent.** Each set of data points is a compilation of five runs. The current is 50 nA, and the in-plane field is 8T. Data is from Device 1, from the same measurement session as that for Figure 2.

**S9. Evidence against current-induced vortex motion as cause of signal's $cos(2\theta)$ character**

Ref. [36] reports a kink in the R vs. T curves when plotted in semi-log style as characteristic of vortex motion. The lack of kinks in our analogous plots further strengthens the argument against vortex motion as the primary cause of our signal's character.

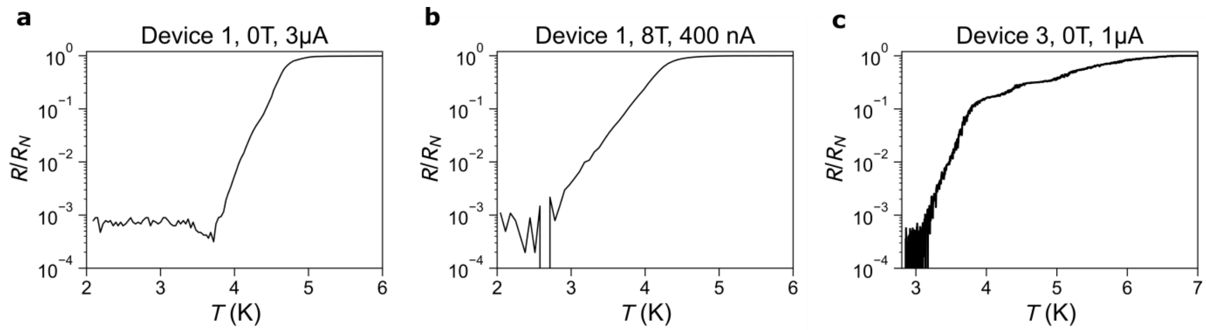


**Figure S9. Evidence against vortex motion.** R vs. T plotted on a semi-log scale. **a.** Device 1, $\mu_0$H = 0T, 3μA. **b.** Device 1, $\mu_0$H = 8T, 400 nA. **c.** Device 3, $\mu_0$H = 0T, 1 μA. In all cases, a characteristic tail due to vortex motion is not seen, ruling out current-induced vortex motion (cf. Fig. 2 in Ref. [36]).

**S10. Differential conductance measurement schematics**

Figure S10 shows the setup for measuring the differential conductance of the junction highlighted by a red square. We use a lock-in amplifier and voltage source meter as the a.c. and d.c. voltage source, respectively. Each instrument is connected to a load resistance to convert the voltage signal to a current signal. A typical d.c. and a.c. load resistance is 100 kΩ and 1MΩ, respectively. The superimposed a.c. and d.c. current is fed to one of the split electrodes. The a.c. and d.c. voltage signal is measured between the other split electrode and another remote electrode. The differential conductance is defined as the ratio of the applied ac current to the measured ac voltage. We normalize the differential conductance G to the zero bias differential conductance in the normal metal state $\mathrm{G_N}$ measured at *T*≈ 5.8 K. All spectra reported are plotted in terms of $\mathrm{G/G_N}$ vs. the measured d.c. bias voltage.

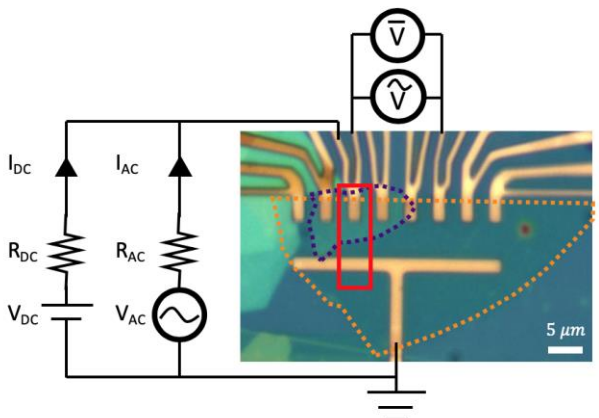


**Figure S10. Schematic of differential conductance measurement.**

**S11. Differential conductance measurements on tunnel junctions with Co/Pt tunnel electrodes**

We present a second device which is constructed with a magnetic metal electrode (multilayer Co/Pt) which also shows a two-fold cos(2θ) modulation, as the one introduced in the main text. Pre-patterned magnetic metal electrodes are prepared by standard photolithography on a Si/$SiO_2$ (290 nm) substrate and e-beam evaporation of 3 nm Ti/10 nm Pt/(0.3 nm Co/1 nm Pt)×8/0.5 nm Co/2.5 nm Au/0.4 nm $AlO_x$, with the $AlO_x$ being on the $NbSe_2$ to form a barrier. Multilayer Co/Pt is a ferromagnetic metal with an easy-axis in the out-of-plane direction [S1]. The measured saturation field for the out-of-plane and in-plane direction is approximately 0.5 T and 0.8T, respectively. The 2.5 nm Au prevents oxidation of Co. A trilayer $NbSe_2$ flake and a h-BN protection layer is transferred in sequence on to the prepatterned substrate by the standard dry transfer technique (Figure S11.1a). The normal state resistance of the junction is $R_N$ = 11 Ω, which is more than an order of magnitude smaller than the $CrBr_3$ barrier device.

We repeat the measurement as introduced in the main text. An in-plane magnetic field of 3T is applied which saturates magnetic moment of the Co/Pt electrodes in the in-plane direction. Differential conductance spectra are acquired as the magnetic field is rotated in the in-plane direction. The results are summarized in Figure S11.1b. Consistent with the main text, there is a two-fold dependence of the spectra in terms of the angle θ. The zero-bias normalized conductance $G/G_N$ vs. angle θ shows a cos(2θ) dependence, while at larger bias the dependence is weak. When the in-plane field is applied along θ = 0°, the differential conductance at sub-gap bias values is suppressed quickly as the field is increased, similar to Figure 3c in the main text. On the other hand, when the field is directed along θ = 70° ($G_N$ maximized), the tunneling spectra shows little dependence on the applied field, as observed in Figure 3d. We find that tunneling to $NbSe_2$ either through a magnetic insulating barrier ($CrBr_3$) or from a magnetic electrode (Co/Pt) results in a similar two-fold modulation of the tunneling spectra. Importantly, the conductance extrema occur near θ = 0°, 180° (field along the long straight edge of the $NbSe_2$ flake) (Fig. S11.1), which is comparable to the results in the magneto-transport (non-magnetic) devices (such as Device 1) where the resistance minima occur when the field is applied parallel to the long straight edge. This could be due to strain associated with this direction induced during the sample preparation process. Note that during the preparation process, three edges of the $NbSe_2$ flake were torn (except for the right straight edge) through a polymer stamp to cut the flake to shape.

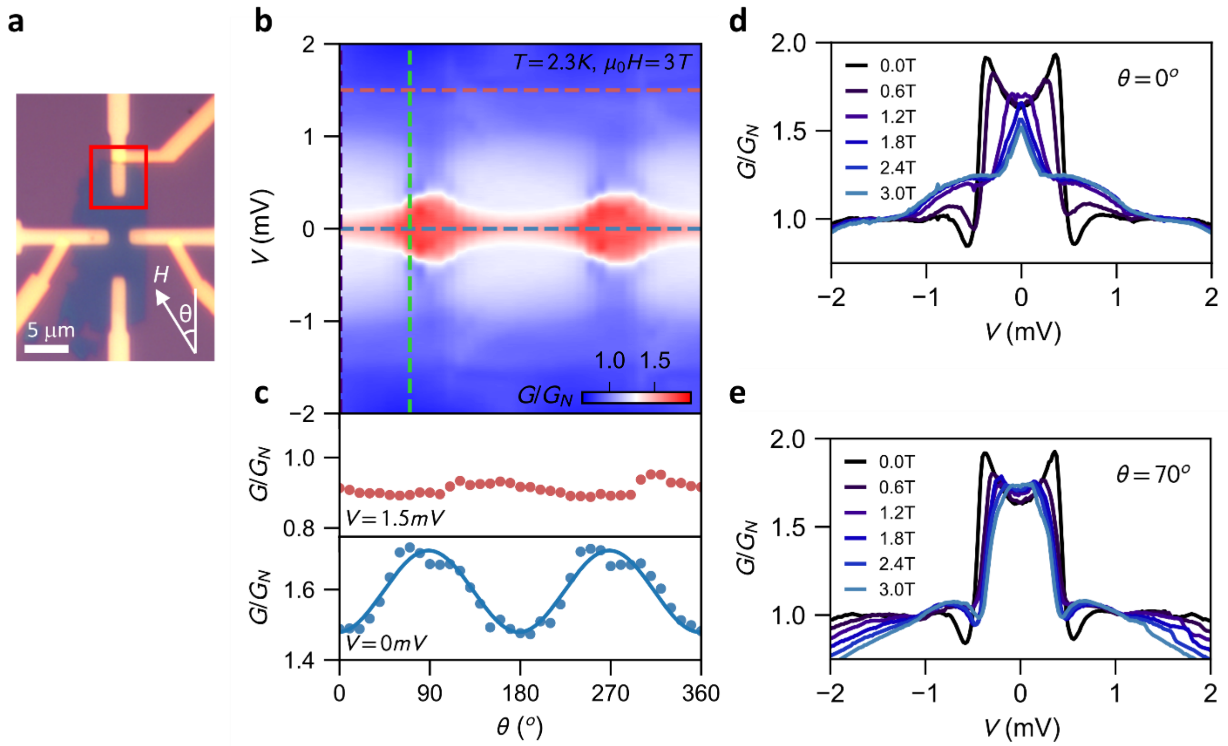


**Figure S11.1. Differential conductance measurement on Device 4. a**. Optical image of Device 4. The visible prepatterned electrodes are multilayers of Co/Pt. The blue flake is a trilayer $NbSe_2$ and the covering h-BN is not shown in this image. The tunnel junction is outlined in red. The in-plane magnetic field angle $\theta$ is defined as illustrated. All edges of the $NbSe_2$ flake except for the right edge were intentionally torn using a stamping technique in order to cut them to shape. **b.** Contour plot of the differential conductance spectra under in-plane magnetic field at 2.3 K. **c.** $G/G_N$ vs. angle at $V = 0$ and 1.5 mV (blue and red dashed lines in **b**). The solid line is the best fit to a cos(2θ) form. **d, e**. Field-dependent differential conductance spectra at two fixed in-plane field directions: θ = 0° (**d**, purple dashed line in **b**) and 70° (**e**, green dashed line in **b**). Results qualitatively similar to those in this figure are observed consistently in other such devices (see Fig. S11.2).

An additional magnetic electrode tunnel device (Device 7) shows consistent results. In this sample, the differential conductance also shows the two-fold cos(2θ) modulation, with the field directions of conductance extrema aligning with the long, straight edge of the flake (Fig. S11.2). The $NbSe_2$ flake edges of Device 7 are as-is from the exfoliation process.

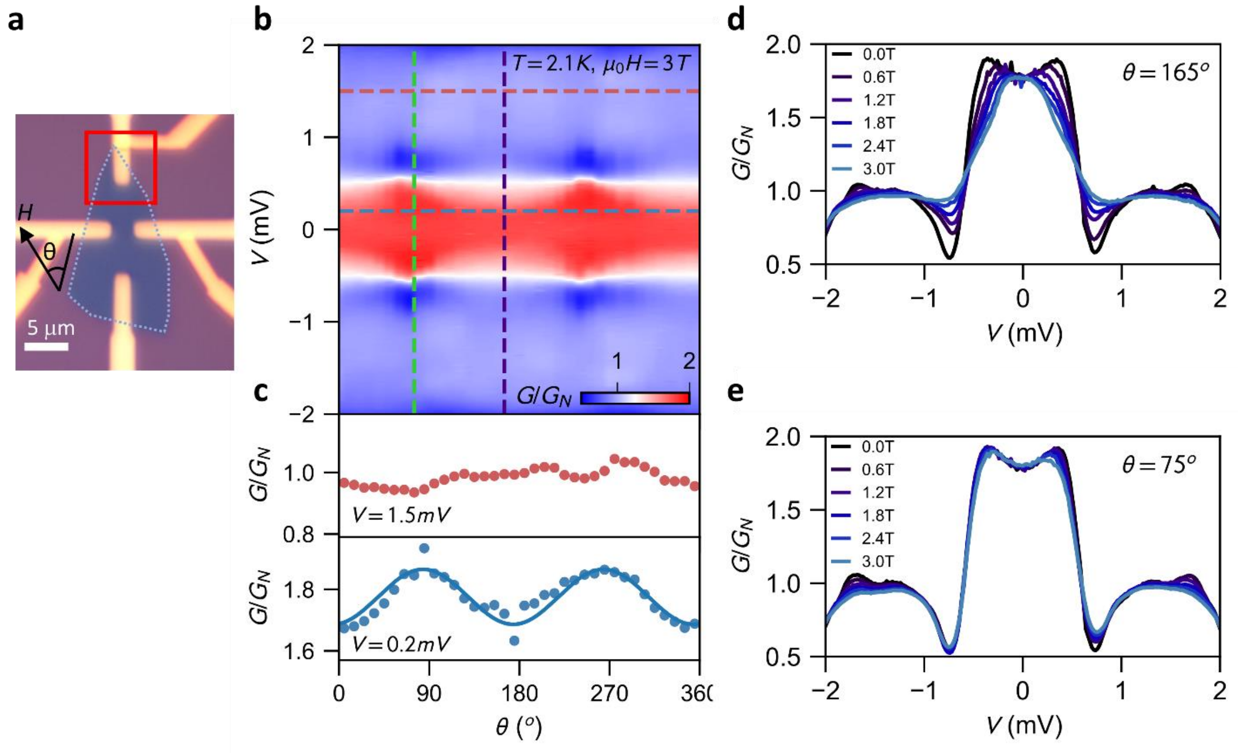


**Figure S11.2. Differential conductance measurements on Device 7. a.** Optical image of Device 7. The visible prepatterned electrodes are multilayers of Co/Pt, with the measured tunnel junction outlined in red. The blue flake in the electrode region is a trilayer $NbSe_2$, and the covering h-BN is not shown in this image. **b.** Contour plot of the differential conductance spectra of device 7 under a 3T in-plane magnetic field at 2.1 K. **c.** $\mathrm{G/G_N}$ vs. $\theta$ at low and high bias fields (blue and red dashed lines in **b.** The solid line is the best fit to a cos(2θ) form. **d, e.** Field-dependent differential conductance spectra for Device 7 at two fixed in-plane field directions.

## S12. Phenomenological Description of Superconducting Anisotropy in $NbSe_2$

Since we expect the behavior of few-layer $NbSe_2$ to be representative of the monolayer compound, as long as the inter-layer coupling is weak, we consider the point group of the latter, which is $D_{3h}$. This point group is non-centrosymmetric, reflecting the fact that it incorporates the effects of the Ising spin-orbit coupling (SOC). In addition, the presence of the substrate breaks the horizontal mirror symmetry of

$D_{3h}$, resulting in an additional Rashba SOC that reduces the point group symmetry to $C_{3v}$. We consider Rashba SOC along with magnetic field and strain as symmetry breaking perturbations and analyze the system from the point of view of $D_{3h}$ symmetry.

The possible superconducting gaps, which we denote $\widetilde{\Delta}^{(\alpha)}_{\Gamma,m}$, can be classified based on the irreducible representation $\Gamma$ of $D_{3h}$ under which they transform, as well as whether they correspond to spin-singlet ($\alpha = s$) or to spin-triplet ($\alpha = t$) Cooper pairs. When $\Gamma$ is not one-dimensional, we use the index $m$ to distinguish different components of the corresponding multiplet. We note that since $D_{3h}$ incorporates Ising SOC, a given $\Gamma$ contains both singlet and triplet gap components, and the solutions of the superconducting gap equation are a mixture of spin-singlet and spin-triplet Cooper pairs[18,23,25]

| $\Gamma$ | $m$ | $\Theta^{(s)}_{\Gamma,m}(\mathbf{p})$ | $\Theta^{(t)}_{\Gamma,m}(\mathbf{p})$ |
|---|---|---|---|
| $A_1'$ | 1 | $i\sigma^y$ | $\cos 3\theta_k\, \sigma^z i\sigma^y$ |
| $E'$ | 1 | $\cos 2\theta_k\, i\sigma^y$ | $\cos\theta_k\, \sigma^z i\sigma^y$ |
| | 2 | $\sin 2\theta_k\, i\sigma^y$ | $\sin\theta_k\, \sigma^z i\sigma^y$ |
| $E''$ | 1 | | $\cos 3\theta_k\, \sigma^x i\sigma^y$ , $(\cos\theta_k\, \sigma^x - \sin\theta_k\, \sigma^y) i\sigma^y$ |
| | 2 | | $\cos 3\theta_k\, \sigma^y i\sigma^y$ , $(\sin\theta_k\, \sigma^x + \cos\theta_k\, \sigma^y) i\sigma^y$ |

**Table S12. Irreducible representations of $D_{3h}$ relevant to our analysis.** We exclude irreps that vanish in the monolayer ($p_z = 0$) limit. The singlet component of $A_1'$ ($E'$) can be associated to an $s$-wave ($d$-wave) gap, while the lowest harmonic in the triplet $E''$ irrep can be associated with a $p$-wave order parameter. Here we take one of the $K$ points to lie along the $p_x$ axis, i.e. $\theta_k = 0$.

Here we focus on the $\Gamma$ pocket (not to be confused with the irrep index), since we expect the gap associated with $\pm K$ pockets to be isotropic[25]. The corresponding superconducting gap $\widetilde{\Delta}(\mathbf{p})$ can then be expressed as:

$$\widetilde{\Delta}(\mathbf{p}) = \sum_{\Gamma\alpha m} \Theta^{(\alpha)}_{\Gamma,m}(\mathbf{p}) \Delta^{(\alpha)}_{\Gamma,m} \tag{1}$$

where $\Delta_{\Gamma,m}^{(\alpha)}$ is a complex scalar parameterizing the magnitude of the contribution to the superconducting gap from the irrep $\Gamma$, in pairing channel $\alpha$. We take $\Theta_{\Gamma,m}^{(\alpha)}(\mathbf{p})$ to be functions of only the angle $\theta_k$ with respect to the Brillouin zone center. Note that by particle hole symmetry, $\widetilde{\Delta}(\mathbf{p}) = -\widetilde{\Delta}^T(-\mathbf{p})$, which implies that $\Theta_{\Gamma,m}^{(s)}(\mathbf{p})$ ($\Theta_{\Gamma,m}^{(t)}(\mathbf{p})$) is an even (odd) function of $\mathbf{p}$.

The irreps relevant to our analysis here are shown in Table S12. To make a connection with the usual classification of gaps in isotropic space, we note that these are an $s$-wave singlet gap and $f$-wave triplet gap in the $A_1'$ irrep; a $d$-wave singlet and a $p$-wave triplet in the $E$' irrep; and $p$-or $f$-wave triplets in the $E$'' irrep. We have omitted most irreps corresponding to gaps that are non-uniform on the $K$ pockets, which do not contribute to the leading-order superconducting instabilities.[25] The exception is the $E$' irrep, which we keep because it couples to $A_1'$ by strain, and the $p$-wave gap in the $E$'' irrep, which can couple to the magnetic field, as these can generate a two-fold anisotropy in the superconducting gap. We have also kept only irreps relevant to the monolayer limit (i.e. independent of the $\hat{z}$ direction). Note that a gap that transforms as any irrep other than $A_1'$ breaks the point group symmetry, but only the gaps transforming as the $E'$ and $E''$ irreps can break the three-fold rotational symmetry of $D_{3h}$.

A few remarks are in order. First, because of the Ising spin-orbit coupling, the $A_1'$ and $E$' irreps contain both singlet and triplet gaps. The $E$'' irrep, however, contains only triplet components as the corresponding singlet gap cannot be realized in a $\hat{z}$-independent way. Second, the $E$' and $E$'' irreps are 2-dimensional, leading to two degenerate solutions to the gap equation. Third, the two different options for $E''$, - *f*-wave, with pre-factor $cos(3\theta_k)$ and *p*-wave, with pre-factor $cos(\theta_k)$, - must necessarily be either both zero or both non-zero, since they transform as the same irrep. In what follows, we focus only on the contribution of the *p*-wave component of $E''$, since the *f*-wave component only gives a six-fold anisotropy of the gap, which is already present in the trivial $A_1'$ channel.

In order to determine the form of the superconducting gap in the presence of strain and a magnetic field, we use a phenomenological approach, analyzing what terms quadratic in the superconducting gaps are allowed in the Ginzburg-Landau free energy. Within this approach the functional form of the gap is not determined, only the relative weights of each irrep. If an irrep has a non-zero weight, in general all terms (including singlet and triplet terms) transforming as that irrep are present in the solution. Usually, only one of the terms within a given irrep in Table S12 is dominant, and the rest can be neglected. Here we focus on what we expect to be the dominant terms that generate two-fold anisotropic spectra, namely: the singlet component of the gap in $A_1'$ (*s*-wave), the singlet *d*-

wave term in $E'$, and the triplet $p$-wave term in $E''$. We can therefore drop the superscript on the coefficients in front of the gap function within a given irrep and label them as $\Delta_{A_1'}$, $\mathbf{\Delta}_{E'}$ and $\mathbf{\Delta}_{E''}$, where the latter are 2-component vectors representing the two-dimensional irreps.

We assume that the dominant superconducting instability is in the $A_1'$ irrep, which contains singlet $s$-wave terms. Near the superconducting transition temperature (in the absence of a magnetic field or strain), the free energy has the form

$$\mathcal{F}_0 = \mathcal{F}_0\left[\Delta_{A_1'}\right] + \frac{1}{2}\left(\chi_{E'}^{-1}(T)|\mathbf{\Delta}_{E'}|^2 + \chi_{E''}^{-1}(T)|\mathbf{\Delta}_{E''}|^2\right)\ . \tag{2}$$

Here $\chi_\Gamma(T) \propto 1/(T - T_{c,\Gamma})$ is the susceptibility associated with superconducting fluctuations in the $\Gamma$ irrep, with $T_{c,\Gamma}$ being the corresponding transition temperature. We leave here the precise form of $\mathcal{F}_0\left[\Delta_{A_1'}\right]$ unspecified. Our main assumption is that the leading superconducting instability takes place at a temperature $T_{c,A_1'}$ that is larger than $T_{c,E'}$ and $T_{c,E''}$. This is in agreement with the microscopic theory that finds a dominant $A_1'$ gap at zero magnetic field [25].

In the presence of perturbations such as strain and magnetic field, which do not respect the $D_{3h}$ symmetry, additional terms in the free energy that mix the different irreducible representations at quadratic order in the $\Delta_{\Gamma,m}$ are allowed. We consider two mixing terms that can lead to a twofold anisotropy in the superconducting gap.

First, since the in-plane magnetic field $\mathbf{b}$ (in units of the Bohr magneton times the Landé g-factor, $\mathbf{b} = \frac{1}{2}g_L\mu_\mathrm{B}\mathbf{B}$) transforms according to the $E''$ irrep and the Ising spin-orbit coupling vector $\lambda p_F^3\cos 3\theta_k\hat{\mathbf{z}}$ transforms according to $A_1'$, a singlet $A_1'$-triplet $E''$ mixing term of the form $\lambda p_F^3\Delta_{A_1'}\mathbf{b}\cdot(\hat{z}\times\mathbf{\Delta}_{E''})$ is allowed, consistent with the results of Ref. [17]. The resulting term in the free energy is

$$\mathcal{F}[\Delta_{A_1'}, \mathbf{\Delta}_{E''}] = \lambda_1 \mathrm{Re}\left[\Delta_{A_1'}^*\left(b_y\Delta_{E'',1} - b_x\Delta_{E'',2}\right)\right]\ . \tag{3}$$

where $\lambda_1$ is some coupling constant proportional to $\lambda$. Minimizing the resulting free energy with respect to $\Delta_{E'',m}$, we find that

$$(\Delta_{E'',1}, \Delta_{E'',2}) = -\lambda_1\chi_{E''}\Delta_{A_1'}(b_y, -b_x) \tag{4}$$

and the total superconducting gap is

$$\widetilde{\Delta}(\mathbf{p}) = \Delta_{A_1'}\left[\Theta_{A_1'}(\mathbf{p}) - \lambda_1\chi_{E''}\mathbf{\Theta}_{E''}(\mathbf{p})\cdot(\hat{z}\times\mathbf{b})\right] \tag{5}$$

which is a mixture of the $s$-wave singlet $A_1'$ gap and the $p$-wave triplet $E''$ gap. Note that since the magnetic field breaks the $D_{3h}$ symmetry, it also lifts the degeneracy between the two components of the $E''$ gap, selecting a real admixture between them. The magnitude of $\Delta_{E''}$ (relative to that of $\Delta_{A_1'}$) is set by the coefficient $\lambda_1 \chi_{E''}|b|$. Since the magnetic field $b$ is a small perturbation, generically we expect this coefficient to be small, and the corresponding mixing to be weak. However, if $T_{c,E''}$ is comparable to $T_{c,A_1'}$, then in the vicinity of $T_{c,A_1'}$ the susceptibility $\chi_{E''}(T) \sim 1/(T_{c,A_1'} - T_{c,E''})$ is very large. Thus we expect that weak magnetic fields can lead to appreciable mixing between the $s$-wave singlet and the $p$-wave triplet only when $T_{c,A_1'}/T_{c,E''}$ is close to 1, i.e. only when these two superconducting instabilities are close competitors.

Second, the strain combination $\boldsymbol{\mathcal{E}} = (\varepsilon_{xx} - \varepsilon_{yy}, 2\varepsilon_{xy})$ transforms according to the $E'$ irreducible representation. Here, $\varepsilon_{ij} \equiv \frac{1}{2}(\partial_i u_j + \partial_j u_i)$ is the strain tensor and $\mathbf{u}$ is the displacement vector. This leads to a coupling between the singlet components of the $A_1'$ and $E'$ gaps of the form:

$$\mathcal{F}[\Delta_{A'_1}, \boldsymbol{\Delta}_{E'}] = \lambda_2 \left[(\varepsilon_{xx} - \varepsilon_{yy})\mathrm{Re}\left(\Delta^*_{A_1'}\Delta_{E',1}\right) + 2\varepsilon_{xy}\mathrm{Re}\left(\Delta^*_{A_1'}\Delta_{E',2}\right)\right] . \tag{6}$$

where $\lambda_2$ is some coupling constant. Minimizing the free energy leads to a mixed $s$-wave and $d$-wave superconducting gap

$$\widetilde{\Delta}(\mathbf{p}) = \Delta_{A_1'}\left[\Theta_{A_1'}(\mathbf{p}) - \lambda_2 \chi_{E'} \boldsymbol{\Theta}_{E'} \cdot \boldsymbol{\mathcal{E}}\right] \tag{7}$$

Again, small strains will only lead to a significant $E'$ component in the superconducting gap if the $A_1'$ and $E'$ superconducting instabilities have similar transition temperatures.

Fig. 4**a**-**c** of the main text shows the resulting momentum-space 2-fold anisotropy in the superconducting gap around the $\Gamma$ pocket. We obtained the plots using a simple model of the single-body Hamiltonian in momentum space:

$$H(\mathbf{p}) = \sum_{\mathbf{p}s} \varepsilon(\mathbf{p}) c^\dagger_{\mathbf{p}s} c_{\mathbf{p}s} + \sum_{\mathbf{p}ss'} c^\dagger_{\mathbf{p}s}[\lambda p_F^3 \cos 3\theta \sigma^z + \mathbf{b}\cdot\boldsymbol{\sigma}]_{ss'} c_{\mathbf{p}s'} = \sum_{\mathbf{p}ss'} c^\dagger_{\mathbf{p}s}[\mathcal{H}_0]_{ss'} c_{\mathbf{p}s'} \tag{8}$$

where $s$ and $s'$ are spin indices,

$$\varepsilon(\mathbf{p}) = -\frac{p^2}{2m} - \mu, \tag{9}$$

and $\theta$, as above, is the angle measured from the center of the $\Gamma$ pocket with $\theta_k = 0$ corresponding to the direction towards the $K$ point. We use $\lambda p_F^3 = 40$ meV, which is the Ising SOC value reported in the literature once averaged over all Fermi surfaces.[14] We also set $\mu = 0.4$ eV, which gives $m = p_F^2/2\mu \approx 2m_0$ when the wavenumber corresponding to the Fermi momentum is $p_F/\hbar = 0.45$ Å$^{-1}$ [S2]. Here, $m_0$ is the electron rest mass. All these parameters were chosen so that the Fermi surface of the toy-model parabolic dispersion is similar to that obtained from first principle calculations[14,18,23].These values should thus not be understood as actual parameters that a first-principle calculation would yield. The key point is that our conclusions do not rely on this set of parameter values, as they are used to illustrate the two-fold gap anisotropy that must follow from mixing an $A_1'$ gap with either $E$' or $E$'' gaps. Finally, for the magnetic field, we use $b = 0.5$ meV, which is about 8.3 T.

The superconducting excitation spectrum is then given by the eigenvalues of the Bogolyubov-de Gennes (BdG) Hamiltonian:

$$H_{BdG} = \frac{1}{2}\sum_{\mathbf{p}} \Psi_{\mathbf{p}s}^{\dagger}\mathcal{H}(\mathbf{p})\Psi_{\mathbf{p}s'} \tag{10}$$

where we use the Nambu-Gor'kov representation $\Psi_{\mathbf{p}s} = (c_{\mathbf{p}s}, c_{-\mathbf{p}s}^{\dagger})^T$ and

$$\mathcal{H}(\mathbf{p}) = \begin{pmatrix} \mathcal{H}_0(\mathbf{p}) & \widetilde{\Delta}(\mathbf{p}) \\ \widetilde{\Delta}^{\dagger}(\mathbf{p}) & -\mathcal{H}_0^T(-\mathbf{p}) \end{pmatrix}. \tag{11}$$

We took $\widetilde{\Delta}(\mathbf{p})$ as in Eqs. (5) and (7). We took the singlet $d$-wave term for $E$' and the triplet $p$-wave term for $E$'' from Table S12. For all plots, we took $\Delta_{A_1'} = 1$ meV (on the order of $T_c$). For the mixed $A_1'/E$' gaps, we took $|\mathbf{\Delta}_{E'}| = 0.1$ meV and an uniaxial strain along the $x$ axis, $\boldsymbol{\mathcal{E}} \propto (1,0)$. For the mixed $A_1'/E$'' gap, the mixing is relatively weak unless the mixed gaps are close in magnitude; for this reason, we used $|\mathbf{\Delta}_{E''}| = 0.5$ meV in the plot. We also set the field to be parallel to the $x$-axis. Note that we plot the energy gap in the spectrum of $H_{BdG}$ (i.e. difference between bottom positive energy band and top negative energy band) along both the inner and outer Fermi surfaces. The resulting gaps on the inner and outer surfaces are identical within the resolution of the figure in panels **a**-**c**.

Although the above mechanism gives a two-fold anisotropy of the superconducting gap in momentum space, the BdG electronic spectrum is insensitive to the direction of the magnetic field. However, one important ingredient missing in the model is the existence of a substrate, which breaks the horizontal mirror symmetry and lowers the point group from $D_{3h}$ to $C_{3v}$. As a result, a Rashba SOC term appears in the Hamiltonian (see for instance Ref. [25]):

$$\mathcal{H}_R = \alpha_R(p_y\sigma^x - p_x\sigma^y) \tag{12}$$

The main effect of this term is to make the BdG spectrum dependent on the direction of the applied field. To illustrate this effect, we plot in Fig. 4 **d**-**f** of the main text the dependence of the minimum gap value on the direction of the magnetic field, highlighting its two-fold anisotropy when Rashba SOC is present (solid lines) and its insensitivity to the field direction when Rashba SOC is absent (dashed lines). For concreteness, we set $\alpha_R p_F = 0.2$ meV -- for comparison, $\alpha_R p_F$ was estimated to be about 0.8 meV in gated $MoS_2$ in [S3]. Note that the Fermi surface is no longer symmetric under momentum inversion in the presence of both Rashba SOC and external magnetic fields[25].

Finally, another potential source of anisotropy comes from the spatial variations of the doublet gaps in the $E'$ and $E''$ irreps, i.e. from the gradient terms of the Ginzburg-Landau free-energy. For the one-component $A_1'$ irrep, the only allowed gradient term is of the form $\mathcal{F}_\nabla^{(A_1')} = K_0 |\nabla D^{(0)}|^2$, which is clearly rotationally invariant. For the doublet $E'$ and $E''$ representations, however, the possible terms in $\mathcal{F}$ involving gradients of the gap functions are [S4]:

$$\mathcal{F}_\nabla^{(\Gamma)} = K_1 |\nabla \cdot \mathbf{\Delta}_\Gamma|^2 + K_2 |\nabla \times \mathbf{\Delta}_\Gamma|^2 + K_3 \left( |\partial_x \Delta_{\Gamma,1} - \partial_y \Delta_{\Gamma,2}|^2 + |\partial_x \Delta_{\Gamma,2} + \partial_y \Delta_{\Gamma,1}|^2 \right) \tag{13}$$

where $\Gamma = E', E''$. These terms can be understood as corresponding to the scalar, (axial) vector, and tensor components of the total derivative $\nabla \mathbf{\Delta}$, assuming no $z$ dependence. Fourier transforming this expression, it follows that, in the presence of an external symmetry-breaking field such as strain, the total gradient term is invariant only under a two-fold rotation with respect to the z-axis[42].

**References:**

[S1]: Lin, C.-J. *et al.* Magnetic and structural properties of Co/Pt multilayers. J. Magn. Magn. Mater **93**, 194 (1991).

[S2]: Borisenko, S. V. *et al.* Two energy gaps and fermi-surface 'arcs' in NbSe2. *Phys. Rev. Lett.* **102**, 166402 (2009).

[S3]: Lu, M. *et al.* Evidence for two-dimensional Ising superconductivity in gated $MoS_2$. Science **350**, 1353 (2015)

[S4]: Sigrist, M. & Ueda, K. Phenomenological theory of unconventional superconductivity. *Rev. Mod. Phys.* **63**, 239–311 (1991).